



Strontium-free rare earth perovskite ferrites with fast oxygen exchange kinetics: Experiment and theory

Christian Berger^a, Edith Bucher^{a,*}, Andreas Windischbacher^b, A. Daniel Boese^b, Werner Sitte^a

^a Montanuniversität Leoben, Franz-Josef-Straße 18, 8700 Leoben, Austria

^b Institute of Chemistry, Karl-Franzens-Universität Graz, Heinrichstraße 28, 8010 Graz, Austria

ARTICLE INFO

Keywords:

Lanthanum calcium ferrite
Praseodymium calcium ferrite
Solid oxide fuel cell cathode
Crystal structure
Defect chemistry
Oxygen exchange kinetics
Electronic conductivity
Ionic conductivity

ABSTRACT

The Sr-free mixed ionic electronic conducting perovskites $\text{La}_{0.8}\text{Ca}_{0.2}\text{FeO}_{3-\delta}$ (LCF82) and $\text{Pr}_{0.8}\text{Ca}_{0.2}\text{FeO}_{3-\delta}$ (PCF82) were synthesized via a glycine-nitrate process. Crystal structure, phase purity, and lattice constants were determined by XRD and Rietveld analysis. The oxygen exchange kinetics and the electronic conductivity were obtained from in-situ dc-conductivity relaxation experiments at 600–800 °C and $1 \times 10^{-3} \leq p\text{O}_2/\text{bar} \leq 0.1$. Both LCF82 and PCF82 show exceptionally fast chemical surface exchange coefficients and chemical diffusion coefficients of oxygen. The oxygen nonstoichiometry of LCF82 and PCF82 was determined by precision thermogravimetry. A point defect model was used to calculate the thermodynamic factors of oxygen and to estimate self-diffusion coefficients and ionic conductivities. Density Functional Theory (DFT) calculations on the crystal structure, oxygen vacancy formation as well as oxygen migration energies are in excellent agreement with the experimental values. Due to their favourable properties both LCF82 and PCF82 are of interest for applications in solid oxide fuel cell cathodes, solid oxide electrolyser cell anodes, oxygen separation membranes, catalysts, or electrochemical sensors.

1. Introduction

Perovskite-type oxides $\text{ABO}_{3-\delta}$ (with A=rare earth element or acceptor substituent, B=transition metal) represent a well-known class of mixed ionic electronic conductors which are of interest for basic research and various applications [1–3]. For instance, the air electrodes of intermediate temperature (600–800 °C) solid oxide fuel cells (SOFCs) and solid oxide electrolyser cells (SOECs) utilize $(\text{La},\text{Sr})(\text{Co},\text{Fe})\text{O}_{3-\delta}$ perovskites for the efficient conversion of the chemical energy of various fuels into electrical energy [4–6]. Recently, A-site substituted perovskite-type ferrites caused much attention due to their high ionic and electronic conductivities, their chemical stability in reducing atmospheres, relatively low thermal expansion coefficients, and their good long-term chemical stability in sulphur containing atmospheres [7–10]. The series $\text{La}_{1-x}\text{Sr}_x\text{FeO}_{3-\delta}$ (LSF) has been thoroughly studied in terms of defect chemistry [11–13], charge transport properties [14–16], and long term degradation due to different contaminants (Cr, Si, and SO_2) to test SOFC cathodes at operational conditions [17–19]. However, in order to further improve the material properties, as well as the lifespans and reliability of these compounds in technical applications, it is necessary to develop new materials with fast oxygen exchange kinetics and high thermodynamic stability. In this

respect, one possible approach is to minimize the mismatch of the ionic radii of the A-site ions to prevent degradation due to mechanical stress and cation segregation [20]. The ionic radius of Sr^{2+} (XII) (1.44 Å) [21] is much larger compared to La^{3+} (XII) (1.36 Å) [21]. This can lead to the segregation of Sr towards grain boundaries and surfaces in order to relieve mechanical stress [20]. These Sr-enriched areas react with impurities from the gas phase (Cr, Si, SO_2 etc.) forming secondary phases, which inhibit the oxygen reduction process [22–24]. As a promising alternative to reduce the mismatch in the ionic radius, the smaller ion Ca^{2+} (XII) (1.34 Å) [21] can be used instead of Sr in these ferrites to obtain $\text{La}_{1-x}\text{Ca}_x\text{FeO}_{3-\delta}$. Compared to the well-characterized LSF series, only a few investigations on material properties of $\text{La}_{1-x}\text{Ca}_x\text{FeO}_{3-\delta}$ are available so far [25–33]. A study on defect chemistry, mass and charge transport properties, and oxygen exchange kinetics of $\text{La}_{0.9}\text{Ca}_{0.1}\text{FeO}_{3-\delta}$ was recently published [34], as well as an investigation on the long-term stability of $\text{La}_{0.8}\text{Ca}_{0.2}\text{FeO}_{3-\delta}$ in SO_2 containing atmospheres [35]. Especially, only few studies on ferrite-based perovskites with varying A-site composition (other than La and Sr) are available. This is somewhat surprising, since the effects of the nature of the A-site cations on material properties have already been shown for similar solid solutions such as $\text{Ln}_{1-x}\text{Sr}_x\text{CoO}_{3-\delta}$ and $\text{Ln}_{1-x}\text{Sr}_x\text{Co}_{1-y}\text{Fe}_y\text{O}_{3-\delta}$ [36–38].

* Corresponding author.

E-mail address: edith.bucher@unileoben.ac.at (E. Bucher).

The present study reports on the synthesis, crystal structure, defect chemistry, and various material properties (thermal expansion coefficient, electronic and ionic conductivities, oxygen surface exchange and diffusion coefficients) of the Ca-substituted ferrites $\text{La}_{0.8}\text{Ca}_{0.2}\text{FeO}_{3-\delta}$ (LCF82) and $\text{Pr}_{0.8}\text{Ca}_{0.2}\text{FeO}_{3-\delta}$ (PCF82). The influence of the A-site host cation (La^{3+} or Pr^{3+}) is investigated, while keeping the concentration of the A-site substituent (Ca^{2+}) constant. To the best of the authors' knowledge, the current paper contains the first results on the oxygen exchange kinetics of PCF82 at 600–800 °C under conditions close to equilibrium (small pO_2 gradients).

While perovskites containing La and Sr, such as $(\text{La,Sr})(\text{Fe,Co})\text{O}_{3-\delta}$, have been studied before by computational methods [39–41], there have been no similar investigations on the Ca or Pr containing structures. Thus, calculations on $\text{A}_{1-x}\text{Ca}_x\text{FeO}_{3-\delta}$ ($\text{A}=\text{La, Pr}$) were performed simulating similar Ca-content and oxygen nonstoichiometries as the experimental material to support the experiments. We compare the computed perovskite structures and their oxygen migration energies to the experimental data and include thermal effects via the harmonic oscillator approximation.

2. Experimental and computational details

2.1. Sample preparation

$\text{La}_{0.8}\text{Ca}_{0.2}\text{FeO}_{3-\delta}$ (LCF82) and $\text{Pr}_{0.8}\text{Ca}_{0.2}\text{FeO}_{3-\delta}$ (PCF82) powders were synthesized via a sol-gel method (glycine-nitrate-process), starting with 1 M aqueous nitrate solutions prepared from $\text{La}(\text{NO}_3)_3 \cdot 6\text{H}_2\text{O}$, $\text{Pr}(\text{NO}_3)_3 \cdot 6\text{H}_2\text{O}$, $\text{Ca}(\text{NO}_3)_2 \cdot 4\text{H}_2\text{O}$, and $\text{Fe}(\text{NO}_3)_3 \cdot 9\text{H}_2\text{O}$ (all chemicals provided by Sigma Aldrich, analytical grade quality). Stoichiometric amounts of each nitrate-solution were mixed and blended with glycine in the ratio of one mole glycine per mole cation. Similar to the process described in [34], water evaporation lead to the formation of a gel which ignited at approximately 250 °C. The resulting ash was calcined at 1000 °C and ball milled for 24 h to obtain a monomodal particle size distribution with an average particle size of 0.90 μm for LCF82, and 0.77 μm for PCF82, respectively (Fig. S-1, Supplementary material). Cylindrical pellets (length \times diameter $\approx 9 \times 5$ mm) of LCF82 and PCF82 were uniaxially pressed at 5.00 kbar (maximum load 1 t), and sintered at 1100 °C for 2 h. For thermal expansion measurements, the front faces of the sintered cylinders were polished to obtain parallel ends. For conductivity relaxation experiments, as well as electrical conductivity measurements, the powders were isostatically pressed at 3.00 kbar and sintered at 1100 °C for 2 h. Sample densities were determined from the mass and geometry of the sintered pellets. Theoretical densities were obtained from Rietveld refinement (see Table S-1 Supplementary material). The density of the sintered LCF82 sample was 97% of the theoretical density ($\rho_{\text{theor}} = 6.3195 \text{ g cm}^{-3}$). The PCF82 sample exhibited 95% of the theoretical density ($\rho_{\text{theor}} = 6.3181 \text{ g cm}^{-3}$). From these dense samples, thin plates with $5 \times 5 \text{ mm}^2$ cross-section and thicknesses of 200–1300 μm were prepared for measurements of the oxygen exchange kinetics and the electrical conductivity (see Section 2.3). The chemical composition of sintered LCF82 and PCF82 pellets was checked by energy dispersive X-ray spectroscopy (EDX) using an EDX Oxford Instruments detector (model 6272) in an energy range up to 20 keV (see Table S-2 Supplementary material). Three iterations on each sample were measured (neglecting oxygen), to get a good overall estimation on the cation stoichiometries. The measured values of the cation stoichiometry agree well with the theoretical values (nominal composition). Minor deviations between measured and theoretical values could be explained by the measurement uncertainty which is estimated to $\pm (2\text{--}3) \text{ at}\%$.

2.2. Crystallographic and thermal analysis

X-ray diffraction (XRD) of the calcined LCF82 and PCF82 powders was performed with a diffractometer (BRUKER-AXS D8 Advance)

using a Cu K α radiation source operated at 40 kV and 40 mA. The diffractograms were recorded at room temperature with a scanning rate of $0.01^\circ \text{ s}^{-1}$. Lattice parameters were obtained from fitting the peak positions to an orthorhombic unit cell using the computer software MAUD [42].

The thermal expansion of LCF82 and PCF82 was measured in the temperature range of $30 \leq T/^\circ\text{C} \leq 1000$ at heating rates of 1 K min^{-1} in the oxygen partial pressure range of $1 \times 10^{-3} \leq \text{pO}_2/\text{bar} \leq 1$, using a dilatometer (DIL 402/PC4, Netzsch). The cylindrically shaped, sintered sample was 5.1 mm in diameter and 6.9 mm in length for LCF82 and 4.9 mm in diameter and 6.8 mm in length for PCF82.

Differential scanning calorimetry (High Temperature DSC 404C Pegasus® with TASC 414/3 A controller and PU1 power unit) of the sintered LCF82 and PCF82 powder was performed in the range of $20 \leq T/^\circ\text{C} \leq 1000$ at a heating rate of 20 K min^{-1} with an isotherm at 1000 °C for 10 min and a gas flow of 50 ml min^{-1} Ar 5.0.

The oxygen nonstoichiometry of LCF82 and PCF82 was determined by precision thermogravimetry (TG) using a symmetric thermobalance (Setaram model TAG 2416). Small amounts (approx. 50 mg) of the sintered powders were placed in a platinum crucible. Different oxygen partial pressures were adjusted with mass flow controllers (red-y, Vögtlin Instruments AG) using mixtures of O_2 4.5, Ar 5.0, and a test gas of 1% O_2 in Ar. An in-situ oxygen sensor with Ir/IrO₂-reference (Setnag, France) was used to determine the oxygen partial pressure close to the sample during each experiment. Experiments were performed in the isothermal and isobaric mode. The agreement between data from both experimental modes was checked, in order to confirm that all data were acquired under equilibrium conditions. Based on literature data for the similar compounds $\text{La}_{0.8}\text{Ca}_{0.2}\text{FeO}_{3-\delta}$ [25], $\text{La}_{0.8}\text{Sr}_{0.1}\text{FeO}_{3-\delta}$ and $\text{La}_{0.75}\text{Sr}_{0.25}\text{FeO}_{3-\delta}$ [15], and $\text{La}_{0.8}\text{Sr}_{0.2}\text{FeO}_{3-\delta}$ [43] it was assumed that $\delta \rightarrow 0$ at room temperature and $\text{pO}_2 = 0.2 \text{ bar}$ for LCF82 and PCF82.

2.3. Electronic conductivity and conductivity relaxation measurements

The electronic conductivity was measured as a function of temperature and pO_2 by the four-point dc van der Pauw method using a Keithley model 2400 as combined current source and voltmeter. The chemical surface exchange coefficient k_{chem} as well as the chemical diffusion coefficient of oxygen D_{chem} were obtained from in-situ four-point dc-conductivity relaxation experiments which were conducted in van der Pauw electrode configuration [44]. The dense samples had a cross section of approximately $5 \times 5 \text{ mm}^2$ and were contacted with gold wires and gold paste. Platelets with two different thicknesses were used for each material, on the one hand to check the reproducibility of the data, and on the other hand to obtain both k_{chem} and D_{chem} in wider T- and pO_2 -ranges. The thicknesses of the specimens were 503 and 1268 μm (LCF82) and 209 and 502 μm (PCF82). The electrical conductivity responses of the samples to step-wise changes of the oxygen partial pressure were recorded. The kinetic parameters (k_{chem} and D_{chem}) were obtained from nonlinear least squares fits of the solution of the diffusion equation to the conductivity relaxation data [11,45,46]. In order to study the oxygen exchange kinetics close to equilibrium, small pO_2 -steps were performed in the oxygen partial pressure ranges $1.0 \times 10^{-1} - 1.5 \times 10^{-1}$, $1.0 \times 10^{-2} - 1.5 \times 10^{-2}$, and $1.0 \times 10^{-3} - 1.5 \times 10^{-3} \text{ bar}$, in oxidizing and reducing directions using O_2 -Ar mixtures at a constant total gas flow of $2 \text{ dm}^3 \text{ h}^{-1}$.

2.4. Computational details

Experimental [47] as well as computational [48] data of $(\text{La,Sr})\text{FeO}_{3-\delta}$ indicated that a slightly different Sr-content had no effect on formation and migration energies of the oxygen vacancies. Assuming the same behaviour for Ca-containing compounds, the calculations were performed on $\text{A}_{0.75}\text{Ca}_{0.25}\text{FeO}_{3-\delta}$ ($\text{A}=\text{La, Pr}$) structures (indicated

in the following as LCF and PCF) in order to avoid the calculation of much bigger supercells, which would have been required for $\text{A}_{0.8}\text{Ca}_{0.2}\text{FeO}_{3-\delta}$ ($\text{A}=\text{La}, \text{Pr}$). The energy calculations were performed using the Vienna Ab Initio Simulation Package (VASP) [49,50] version 5.4.1. Potentials constructed with the projector-augmented wave (PAW) method as provided by the VASP library [51] were used. Due to convergence problems with the structures containing praseodymium, ‘softer’ VASP potentials of all components were employed for the calculation of PCF. For LCF, both pseudopotentials virtually yielded the same results. All calculations were performed with the exchange correlation functional of Perdew, Burke, and Ernzerhof (PBE) [52], using the D3 dispersion correction [53] with Becke-Johnson damping [54].

An energy cut-off of 600 eV for LCF and of 400 eV for the softer PCF calculation was set. The LCF calculations were carried out using a $4 \times 3 \times 4$ Monkhorst-Pack k-point mesh and the PCF calculations a $4 \times 4 \times 3$ Monkhorst-Pack k-point mesh for the unit cell optimization. To compare computational predictions with experimental data, supercells consisting of 80 and 160 atoms were constructed, requiring $2 \times 3 \times 2$ and $2 \times 2 \times 2$ (LCF) and $2 \times 2 \times 3$ and $2 \times 2 \times 2$ (PCF) Monkhorst-Pack k-point meshes. The energy convergence was set to 10^{-5} eV. We also corrected for zero-point energies and temperature effects by calculating numerical frequencies at the gamma point and using the harmonic oscillator (HO) approximation.

Oxygen migration was examined using the nudged elastic band (NEB) [55] approach for finding the saddle point. Here, we utilized the climbing-image NEB (CI-NEB) method [56,57] as implemented in the VASP 5.2 transition state theory tools from the University of Texas [58].

3. Results and discussions

3.1. Crystal structure

The X-ray diffraction patterns of LCF82 and PCF82 are illustrated in Fig. 1. The lattice constants of the orthorhombic unit cells are given in Fig. S-2 (Supplementary material), in comparison with literature data. Data of the lattice constants, cell volumes, and tolerance factors are summarized in Table 1. Fe-O bond lengths and Fe-O-Fe binding angles are listed in Table 2. All reflections of LCF82 are indexed in orthorhombic perovskite with space group $Pnma$, in analogy to the previously reported structure of $\text{La}_{0.9}\text{Ca}_{0.1}\text{FeO}_{3-\delta}$ (LCF91) [34,62]. The orthorhombic perovskite PCF82 has the space group $Pbnm$ (Fig. 1). Both diffraction patterns and the refined lattice constants (Fig. S-2; Supplementary material) match well with the previously reported data

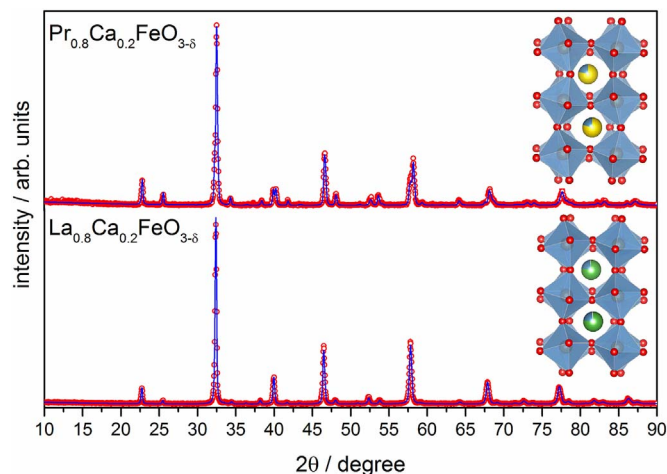


Fig. 1. Powder diffraction patterns (circles) and Rietveld refinement (lines) of LCF82 and PCF82 with the respective crystal structures.

Table 1

Lattice parameters of LCF82 and PCF82 obtained from Rietveld structural refinement in the orthorhombic space group $Pnma$ for LCF82 and $Pbnm$ for PCF82 in comparison with computational results (PBE-D3) and tolerance factors.

| | a / Å | b / Å | c / Å | V / Å ³ | t |
|--------|-----------|-----------|-----------|--------------------|-------|
| LCF82 | 5.5105(3) | 7.7985(4) | 5.5341(3) | 237.8204 | 0.953 |
| PBE-D3 | 5.384 | 7.675 | 5.410 | 223.6 | |
| PCF82 | 5.4787(2) | 5.5433(2) | 7.7726(3) | 236.0544 | 0.903 |
| PBE-D3 | 5.397 | 5.400 | 7.677 | 223.7 | |

Table 2

Selected Fe-O bond lengths and Fe-O-Fe bond angles of LCF82 obtained from Rietveld structural refinement in the orthorhombic space group $Pnma$ for LCF82 and $Pbnm$ for PCF82 in comparison with computational results (PBE-D3).

| | Fe1-O1 / Å | Fe1-O2 / Å | Fe1-O2 / Å | Fe1-O1-Fe1 / ° | Fe1-O2-Fe1 / ° |
|--------|-------------|------------|------------|----------------|----------------|
| LCF82 | 1.98248(10) | 1.99882(8) | 1.98660(8) | 159.1093(16) | 156.9222(10) |
| PBE-D3 | 1.91 | 1.93 | 1.92 | 159.6 | 160.2 |
| PCF82 | 2.00753(8) | 2.00087(6) | 1.98597(6) | 150.9013(15) | 155.6187(7) |
| PBE-D3 | 1.92 | 1.94 | 1.93 | 157.2 | 161.6 |

for LCF82 [59] and PCF82 [33]. In the powder diffractogram of PCF82, peak-splittings are evident at 2θ -values of 39.92° (022), 40.24° (202), 57.70° (132), 57.91° (024), and 58.19° (312) lattice planes. These match reflexions (overlapping due to lower intensity) of LCF82 at 2θ -values of 39.93° (022), 40.02° (220), 57.74° (123) and 57.88° (321) lattice planes. PCF82 is a single phase material, while LCF82 shows approximately 1.5 wt% of a $\text{Ca}_2\text{Fe}_2\text{O}_5$ (brownmillerite) impurity phase evident at $33.56^\circ 2\theta$. However, it is assumed that the small amount of the latter secondary phase has a negligible effect on the material properties of LCF82. The tolerance factor t (Table 1) was calculated according to Eq. (1) to describe the deviation from the ideal cubic perovskite structure [37,60].

$$t = \frac{0.8 r_A + 0.2 r_A' + r_O}{\sqrt{2} (r_B + r_O)} \quad (1)$$

For estimation of t , the following ionic radii from [21] under consideration of coordination number and charge were used: r_A represents $r(\text{La}^{3+})=1.36$ Å, or $r(\text{Pr}^{3+})=1.179$ Å, respectively; r_A' denotes $r(\text{Ca}^{2+})=1.34$ Å; for r_B the value $r(\text{Fe}^{3+}(\text{high spin}))=0.645$ Å was used; r_O is given by $r(\text{O}^{2-})=1.40$ Å. The numerical pre-factors (0.8 and 0.2) describe the site occupancy for A-site substitution in the ABO_3 perovskite system. For the ideal cubic perovskite structure the tolerance factor is unity, whereas LCF82 ($t=0.953$) and PCF82 ($t=0.903$) show slight deviations from the cubic structure towards the orthorhombic structure by tilting of the FeO_6 octahedra (compare also Fig. 1). The t value for PCF82 is lower compared to LCF82. This may be due to the partial oxidation of Fe^{3+} to Fe^{4+} due to electronic charge compensation of the partial substitution of Pr^{3+} with Ca^{2+} , similar to the analogous effect reported for Sr^{2+} substituted perovskites [61]. It has to be mentioned that the calculated tolerance factors assume an ideal cation stoichiometry ($\text{A}:\text{A}':\text{B}=8:2:10$) with the A-site being occupied exclusively by $\text{La}^{3+}(\text{Pr}^{3+})$ and Ca^{2+} and the B-site by Fe^{3+} (high spin). Even though EDX analyses of LCF82 and PCF82 suggest that the actual compositions of the materials are close to the theoretically expected cation stoichiometry (see Table S-2 Supplementary material), the measurement uncertainty of the method is too large to exclude that small deviations in the range of one (or several) tenth atomic percent occur. Further, valence changes, for example from Pr^{3+} to Pr^{4+} , may occur if PCF82 is slightly sub-stoichiometric in CaO , or due to changes in the oxygen nonstoichiometry. In this case, it cannot be excluded that a small amount of Pr^{4+} is incorporated on the B-site. Further, the

valence state of Fe will be affected by changes in the oxygen nonstoichiometry. Due to all these considerations, the tolerance factors of LCF82 and PCF82 given above are to be understood as approximations.

For the computational study, the orthorhombic unit cells obtained from the diffraction experiments were taken and the geometries relaxed. The small deviations of the lattice constants of about –2% as displayed in Table 1 are on the one hand due to thermal expansion and the optimization performed at 0 K (while XRD measurements were done at room temperature), on the other hand they are within the error limit of the functional used. The calculated Fe–O bond lengths and Fe–O–Fe binding angles are shown in Table 2. The good accordance of the lattice constants and the associated binding properties justifies the decision of simplifying the ratio of A (A=La, Pr): O=5:1 to 4:1 and supports the finding in references [47] and [48]. Thus, we decided to use these simplified structures in our further studies.

3.2. Thermal expansion, phase transitions, and oxygen nonstoichiometry

The relative thermal expansion ($\Delta L/L_0$) of LCF82 and PCF82 was measured over a temperature range of $30 \leq T/^\circ\text{C} \leq 1000$ at different oxygen partial pressures $1 \times 10^{-3} \leq p_{\text{O}_2}/\text{bar} \leq 1$, Fig. 2. For each measurement, the samples were heated up to 1000 °C and cooled down (all rates were 1 K min^{-1}) at a given p_{O_2} , followed by an isotherm for 2 h at 30 °C, and a second heating and cooling cycle under identical conditions. Before each experiment, the samples were usually equilibrated in a different p_{O_2} (due to heating and cooling in ambient air during sintering, or due to thermal expansion measurements in a different gas atmosphere). Therefore, non-equilibrium effects may affect the data obtained in the first temperature sweep, especially at low temperatures when oxygen exchange kinetics is slow. In order to minimize errors thus introduced, a second temperature sweep with the same p_{O_2} was performed with all measurements, and the slope of the second heating step was used for calculation of the thermal expansion coefficients (TECs).

Price et al. reported phase transition temperatures for the (La,Ca) $\text{FeO}_{3-\delta}$ system [63], which are also appearing in the case of LCF82 as a change of the slope in the thermal expansion curve (region I and II in Fig. 2). PCF82 shows no such slope changes, when measured under the same conditions. All obtained TECs are listed in Table S-3 (Supplementary material). In region I (which includes the typical operating temperatures of IT-SOFCs and IT-SOECs), thermal expan-

sion coefficients of LCF82 and PCF82 match those of common solid electrolytes like $\text{Ce}_{0.9}\text{Gd}_{0.1}\text{O}_2$ (GDC; $12.5 \times 10^{-6} \text{ K}^{-1}$ [64]) and 8 mol-% yttria-stabilized zirconia (YSZ; $10.8 \times 10^{-6} \text{ K}^{-1}$ [65]). This may be an advantage in the technical application, since similar TECs of the electrolyte and the electrode prevent delamination during heating and cooling of SOFCs and SOECs [66]. LCF82 and PCF82 show significantly lower TECs than the state-of-the-art material $\text{La}_{0.6}\text{Sr}_{0.4}\text{CoO}_{3-\delta}$ ($18.9 \times 10^{-6} \text{ K}^{-1}$ [67]). Therefore, LCF82 and PCF82, as well as the lanthanum calcium ferrites in [68], or $\text{La}_{0.9}\text{Ca}_{0.1}\text{FeO}_{3-\delta}$ ($12.4 \times 10^{-6} \text{ K}^{-1}$ [34]), would result in a much better mechanical stability on YSZ/GDC electrolytes than the Co-containing state-of-the-art IT-SOFC or -SOEC air electrode materials. It has to be mentioned that the expansion shown in Fig. 2 includes contributions of both thermal and chemical expansion. The latter effect is due to the progressive decrease in oxygen stoichiometry with increasing temperature and decreasing oxygen partial pressures. In agreement with the oxygen nonstoichiometry of LCF82 and PCF82 shown in Fig. 3, the slopes of the expansion curves (resp. the TEC values shown in Table S-3; Supplementary material) increase at $T \geq 750$ °C and with decreasing p_{O_2} . Also, in agreement with the higher oxygen nonstoichiometry of LCF82 compared to PCF82 (Figs. 3a and 3f), the TEC of LCF82 at $T \geq 750$ °C is higher than that of PCF82. However, a detailed deconvolution of thermal and chemical contributions to the total expansion is beyond the scope of this study.

The previously mentioned phase transition of LCF82 at the borderline between regions I and II (~ 740 °C) can be assigned to the reversible change from the orthorhombic to the rhombohedral structural modification previously described by Price et al. [63]. Indeed, differential scanning calorimetry (DSC) (Fig. S-3, Supplementary material) shows a phase transition with an onset temperature of approximately 720 °C in Ar. The maximum of the temperature peak occurs at approximately 740 °C, which agrees well with the observed change in the thermal expansion behaviour (Fig. 2; Table S-3 in Supplementary material).

Precision thermogravimetry of LCF82 at $600 \leq T/^\circ\text{C} \leq 900$ and $1 \times 10^{-3} \leq p_{\text{O}_2}/\text{bar} \leq 0.1$ shows that the oxygen nonstoichiometry δ increases with increasing temperature and decreasing oxygen partial pressure (Fig. 3). In the case of PCF82, the oxygen nonstoichiometry could only be determined as a function of p_{O_2} at 900 °C (Fig. 3). At lower temperatures the mass changes of PCF82 upon changes of the oxygen partial pressure were too small to determine reliable values of δ . The oxygen nonstoichiometries of both LCF82 and PCF82 are smaller than those of other SOFC cathode materials with high Co- and/or Sr-content, such as $\text{La}_{0.4}\text{Sr}_{0.6}\text{CoO}_{3-\delta}$ [69,70] and $\text{La}_{0.4}\text{Sr}_{0.6}\text{FeO}_{3-\delta}$ [12,15]. This is due to the higher concentration of A-site substituents in $\text{La}_{0.4}\text{Sr}_{0.6}\text{CoO}_{3-\delta}$ and $\text{La}_{0.4}\text{Sr}_{0.6}\text{FeO}_{3-\delta}$, as well as to the more facile reduction of Co, compared to Fe [15,16,71], leading to ionic charge compensation by the formation of oxygen vacancies ($\text{V}_\text{O}^{\bullet\bullet}$).

To simulate the oxygen nonstoichiometry at working temperature range (Fig. 3), two supercells containing 80 and 160 atoms were created for both structures by expanding the unit cell. Based on recent computational work of references [39], the atoms were arranged in linear chains of calcium surrounded by layers of the correlated rare earth ion, as this conformation is lowest in energy. Removing an oxygen atom of both supercells resulted in oxygen nonstoichiometry of 0.0625 and 0.03125, respectively. These values are slightly larger than the measured ones. To go to smaller nonstoichiometries, the supercells would become even larger and computationally prohibitive. Optimizing the structures, the lattice constants were fixed while allowing for internal ionic relaxation. Both structures were used to calculate the vacancy formation enthalpy as well as the oxygen migration energy. As a small change of δ showed no effect on the energy, the results refer to the 80 atoms structure. Further information on the energies of the two different supercells can be found in the Supplementary section (Table S-4).

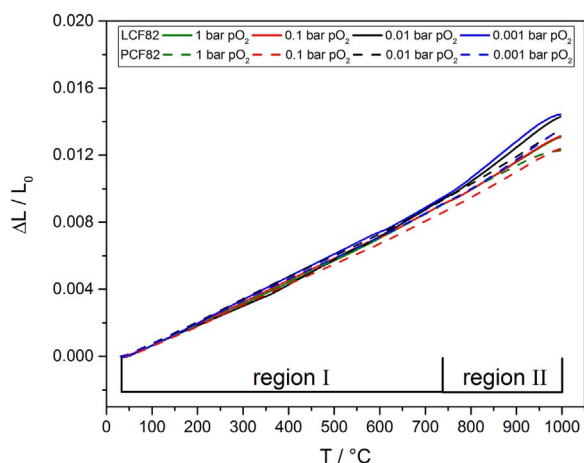


Fig. 2. Expansion curves of LCF82 (note two different temperature regions) and PCF82 (constant slope over the investigated temperature range) at different oxygen partial pressures. The expansion behaviour includes contributions from thermal and chemical expansion.

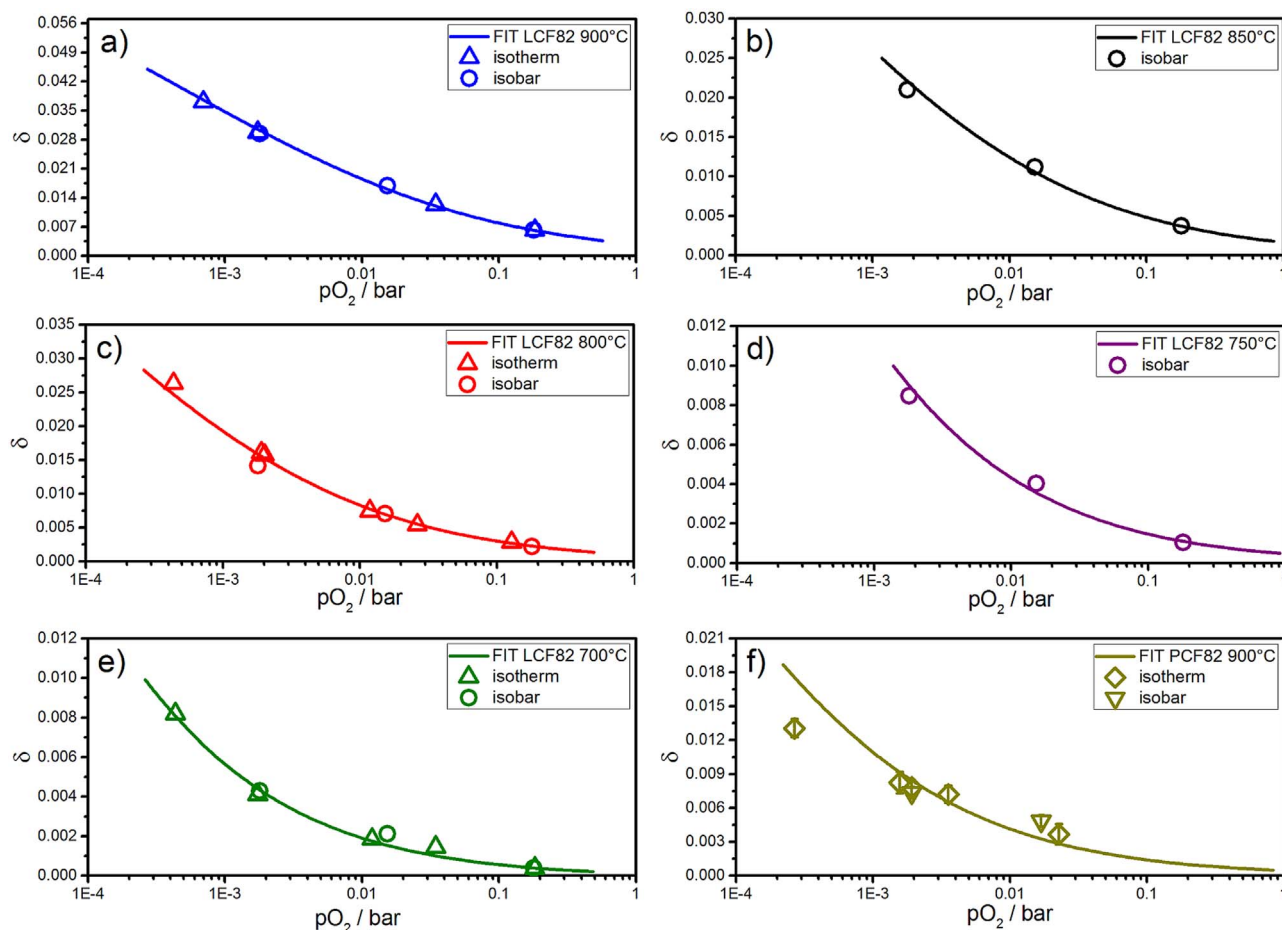


Fig. 3. Oxygen nonstoichiometry as a function of the oxygen partial pressure at different temperatures; a)–e) 900–700 °C for LCF82; f) 900 °C for PCF82; Data points for LCF82 were obtained from isothermal (up triangle) and isobaric measurements (circles). Data points for PCF82 were obtained from isothermal (diamond) and isobaric measurements (down triangle). Lines are nonlinear least squares fits to the defect model (equation 9, [Supplementary material](#)).

3.3. Defect chemical model

The oxygen nonstoichiometry of LCF82 (700–900 °C) and PCF82 (900 °C) can be described by an ideal point defect model, which was developed by Mizusaki et al. [72]. Details on the defect model are given in the [Supplementary material](#). Nonlinear least squares fits of the defect model to the experimental data of δ as a function of pO_2 at various temperatures are shown in [Fig. 3](#). The oxygen nonstoichiometry of LCF82 is described well by the model at $T=700\text{--}900$ °C ([Figs. 3a–3e](#)). In the case of PCF82, deviations occur between data and fit at 900 °C ([Fig. 3f](#)). On the one hand, these deviations may be due to the relatively small weight changes (small δ values in the range of 0.003–0.015) which are thus affected by larger experimental errors, and the limited number of data points available in a relatively narrow pO_2 range. On the other hand, it cannot be excluded that additional effects play a role, such as formation of Pr^{4+} on the A-site and/or incorporation of Pr^{4+} on the B-site. In the latter case, the defect model would have to be adapted in order to consider additional defect species (Pr_{Pr}^{\bullet} , Pr_{Fe}^{\bullet}), the corresponding defect equilibria, and thermodynamic equilibrium constants. However, since there is only a limited number of experimental data points available ([Fig. 3f](#)), and the occurrence of Pr^{4+} on the A- and/or B-site cannot be verified, it would not be justified to apply a more complicated defect model with additional fit parameters.

The equilibrium constants K_{red} , which are obtained as fit parameters from nonlinear regression at various temperatures, are summarized in [Fig. S-4](#) in the [Supplementary material](#) for LCF82 and PCF82. Using K_{red} , the concentrations of the defect species $[Fe_{Fe}^{\bullet}]$, $[O_O^{\bullet}]$, and $[V_O^{\bullet}]$ can be calculated. The pO_2 dependences of the defect

concentrations are plotted in Brouwer diagrams in the [Supplementary material](#) ([Fig. S-5](#) and [Fig. S-6](#)). Due to deviations between data and fit in the case of PCF82 at 900 °C ([Fig. 3f](#)), the value for K_{red} and the Brouwer diagram of PCF82 may be associated with higher uncertainty.

3.4. Electronic conductivity

The electronic conductivities σ_e of LCF82 and PCF82 are given as a function of temperature at different oxygen partial pressures in [Fig. 4a](#). For LCF82 a maximum of the electronic conductivity of $\sigma_e=110\text{ S cm}^{-1}$ is reached at 700 °C and $pO_2=0.1$ bar. In comparison, PCF82 shows $\sigma_e=59\text{ S cm}^{-1}$ under the same conditions. The activation energies for electronic conduction were obtained from the slopes of $\ln(\sigma_e \cdot T)$ vs. T^{-1} plots, and are summarized in [Table 3](#).

As shown in [Fig. 3](#), PCF82 has a lower oxygen nonstoichiometry than LCF82 under comparable experimental conditions. According to the electroneutrality condition (Eqs. (2) and (3), respectively, [Supplementary material](#)), this would mean that PCF82 should have a higher concentration of electron holes (Fe^{4+}) and thus a higher electronic conductivity than LCF82. However, as evident from [Fig. 4a](#) this is not the case, presumably because both LCF82 and PCF82 show relatively small oxygen nonstoichiometries with $2[V_O^{\bullet}] \ll [Fe_{Fe}^{\bullet}]$. This indicates that other factors (chemical nature and valence of A-site host cation, structural parameters etc.) are responsible for the difference in the electronic transport properties of LCF82 and PCF82. Ren et al. [61] showed, by studying various Sr-containing ferrites, that the ionic radius of the A-site host cations has a pronounced effect on the electronic

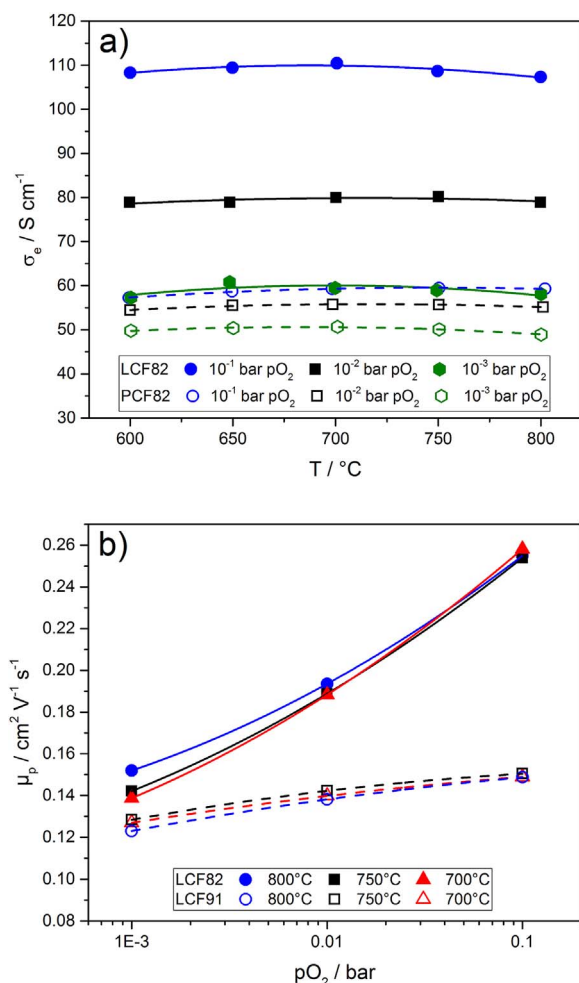


Fig. 4. a) Electronic conductivities of LCF82 and PCF82 as a function of temperature and oxygen partial pressure; b) electronic charge carrier mobilities of LCF82 as a function of the oxygen partial pressure at different temperatures (data of LCF91 [34] are given for comparison); Lines are guides for the eye.

transport properties. $La_{0.8}Sr_{0.2}FeO_{3-\delta}$ and $Pr_{0.8}Sr_{0.2}FeO_{3-\delta}$ [61] show electronic conductivities which are comparable to those of the Ca-containing perovskites LCF82 and PCF82, respectively. This dependence on A-site host cation radius was also previously described for materials with higher alkaline earth metal ion concentration ($x = 0.5$) in the series $Ln_{0.5}Sr_{0.5}FeO_{3-\delta}$ ($Ln = La, Pr, Sm, \dots$) [73]. Electronic conduction in perovskite ferrites is commonly assumed to occur by a small polaron hopping mechanism, which takes place along the Fe-O-Fe pathway [34,74–76]. High electron conduction is possible when the O 2p and Fe 3d orbitals overlap [77,78], which is mainly achieved by certain Fe-O binding distances and Fe-O-Fe angles. These parameters

are listed for LCF82 and PCF82 in Table 2. It is important to consider, that structural distortion (expressed by the deviation of the tolerance factor from unity, Table 1), is decreasing the Fe-O bond length due to an increased overlap between the electron conducting O 2p and Fe 3d orbitals with increasing A-site ionic radius. This has been shown for Sr-doped perovskites and could also be applied to the Ca-doped compounds [61,79–82]. In the case of PCF82, electronic charge compensation may also occur by the oxidation of Pr^{3+} to Pr^{4+} , which is not possible with La^{3+} in LCF82 [61]. This effect may lead to a lower concentration of electron holes (Fe^{4+}) in PCF82 and contribute to the lower electrical conductivity compared to LCF82 [83–85]. In addition to the number of electronic charge carriers, the mobility of the electron holes has an impact on the magnitude of the electronic conductivity. Using the formula unit concentration of the electron holes $p = [Fe^{4+}]$ obtained from the defect model, and the molar volume V_m determined by XRD and Rietveld refinement, the following equation may be used to estimate the mobility of the p-type electronic charge carriers μ_p

$$\mu_p = \frac{\sigma_e V_m}{N_A e p (1 - p)} \quad (2)$$

where N_A is Avogadro's constant and e the elementary charge [14,86]. However, this analysis could only be performed for LCF82, due to the limited data available for $\delta = f(pO_2, T)$ of PCF82 (compare Sections 3.2 and 3.3). The mobilities of electron holes in LCF82 are given as a function of oxygen partial pressure at different temperatures in Fig. 4b. The temperature dependence of μ_p is relatively weak, analogously to the previously studied material $La_{0.9}Ca_{0.1}Fe_{3-\delta}$ (LCF91) [34]. An increase in the electronic charge carrier mobility of LCF82 is found with increasing pO_2 , which may be ascribed to a decrease in the oxygen vacancy concentration (compare Fig. 3). As also described in the detailed investigation on the electronic charge transport properties of LCF91 [34], the presence of oxygen vacancies leads to a decrease in the electronic conductivity which occurs along the Fe-O-Fe pathways in the structure. In comparison with LCF91, LCF82 shows higher electron hole mobilities than LCF91 (Fig. 4b).

3.5. Oxygen exchange kinetics and ionic conductivity

The chemical surface exchange coefficients k_{chem} and the chemical diffusion coefficients D_{chem} of oxygen of LCF82 and PCF82 are given in Fig. 5 and Fig. 6 as a function of temperature at different oxygen partial pressures. A good agreement between oxidation and reduction experiments was observed. It was possible to determine k_{chem} for both materials at $1 \times 10^{-3} \leq pO_2 / bar \leq 0.1$ and $600 \leq T / ^{\circ}C \leq 800$ (Fig. 5). LCF82 shows its highest value for $k_{chem} = 6 \times 10^{-3} cm\ s^{-1}$ at $pO_2 = 0.1$ bar and $T = 800\ ^{\circ}C$. With reducing oxygen partial pressure (from 0.1 to 1×10^{-3} bar pO_2) the values for k_{chem} decrease. A minimum of $k_{chem} = 1 \times 10^{-4} cm\ s^{-1}$ is found at $pO_2 = 1 \times 10^{-3}$ bar. In the lower pO_2 region (from 1×10^{-2} to 1×10^{-3} bar pO_2) PCF82 exhibits faster oxygen surface exchange kinetics than LCF82. Tamimi et al. [87] found similar results for the $Ln_{0.5}Sr_{0.5}Co_{0.8}Fe_{0.2}O_{3-\delta}$ ($Ln = La, Pr, Nd$) series. They

Table 3

Activation energies E_a of various material parameters of LCF82 and PCF82 at different oxygen partial pressures.

| Parameter | LCF82 | | | PCF82 | | |
|----------------|--------------------|---------------------|----------------------|--------------------|---------------------|----------------------|
| | @ $pO_2 = 0.1$ bar | @ $pO_2 = 0.01$ bar | @ $pO_2 = 0.001$ bar | @ $pO_2 = 0.1$ bar | @ $pO_2 = 0.01$ bar | @ $pO_2 = 0.001$ bar |
| σ_e | 8 ± 0.8 | 9 ± 0.2 | 7 ± 0.5 | 9 ± 0.4 | 9 ± 0.7 | 7 ± 0.4 |
| k_{chem} | 99 ± 16 | 94 ± 19 | 134 ± 18 | 138 ± 10 | 97 ± 4 | 69 ± 19 |
| k_O | 110 ± 28 | 74 ± 20 | 83 ± 2 | – | – | – |
| D_{chem} | 97 ± 10 | 85 ± 12 | – | 141 ± 4 | 129 ± 8 | 140 ± 10 |
| D_O | 92 ± 3 | 82 ± 3 | – | – | – | – |
| D_V | 65 ± 10 | 44 ± 8 | – | – | – | – |
| σ_{ion} | 103 ± 1 | 66 ± 1 | – | – | – | – |

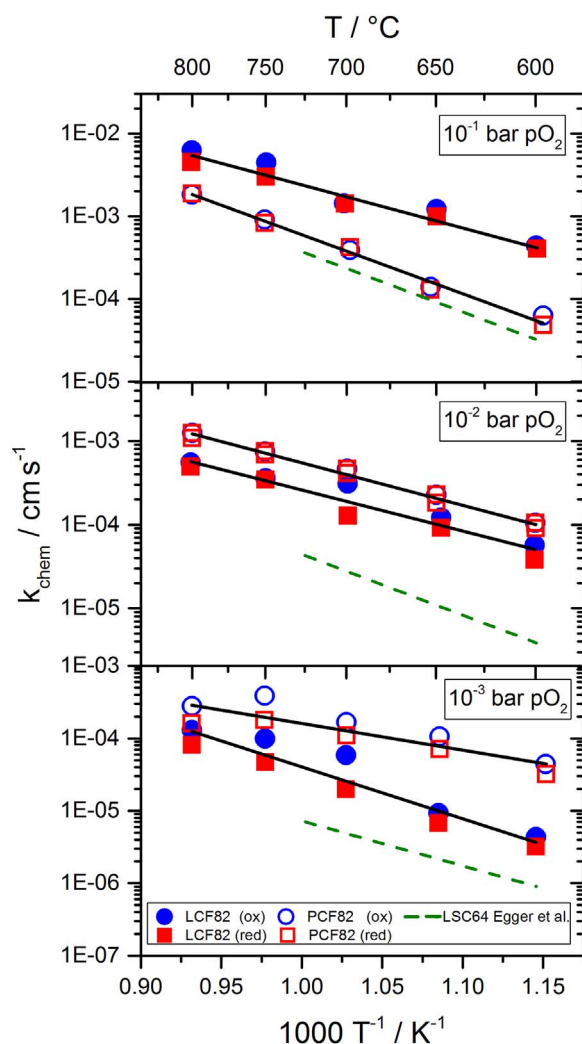


Fig. 5. Arrhenius plots of the chemical surface exchange coefficients (k_{chem}) of LCF82 (solid symbols) and PCF82 (open symbols) at different oxygen partial pressures; the twofold standard deviation of multiple measurements is close to the size of the symbols. For comparison, data of LSC64 from Egger et al. [88] are given (dashed line). Activation energies for k_{chem} of LCF82 and PCF82 are summarized in Table 3. The activation energies for LSC64 are in the range of $114 \leq E_a/\text{kJ mol}^{-1} \leq 155$ [88].

reported higher oxygen exchange rates for $\text{Pr}_{0.5}\text{Sr}_{0.5}\text{Co}_{0.8}\text{Fe}_{0.2}\text{O}_{3-\delta}$ compared to $\text{La}_{0.5}\text{Sr}_{0.5}\text{Co}_{0.8}\text{Fe}_{0.2}\text{O}_{3-\delta}$, which they ascribed to the higher oxygen mobility in the Pr compound.

In comparison with literature data of the well-known SOFC cathode material $\text{La}_{0.6}\text{Sr}_{0.4}\text{CoO}_{3-\delta}$ (LSC64) both LCF82 and PCF82 show significantly higher chemical surface exchange coefficients (Fig. 5). It should be noted that considerable scattering in the values of the oxygen surface exchange coefficients of mixed conducting transition metal oxides is frequently observed with literature data, and even in values determined in the same laboratory. These differences may be due to the preparation and pre-treatment of the samples (purity of the raw materials, thermal history, electrical contacting, measurements setup, etc.). However, since the measurements on LCF82, PCF82, and LSC64, which are compared in this work, were performed in our lab with the same sample preparation methods, same contacting, and in the same experimental setup, the trends observed here should - to the best of the authors' knowledge - be reliable.

Values for D_{chem} were obtained for LCF82 and PCF82 in the temperature range of 600–800 °C and $p\text{O}_2$ range from 0.1 to 0.01 bar (Fig. 6). At 1×10^{-3} bar $p\text{O}_2$ it was only possible to measure D_{chem} for PCF82 from 600 to 700 °C, because at higher temperatures the surface exchange process limits the kinetics. For the same reason,

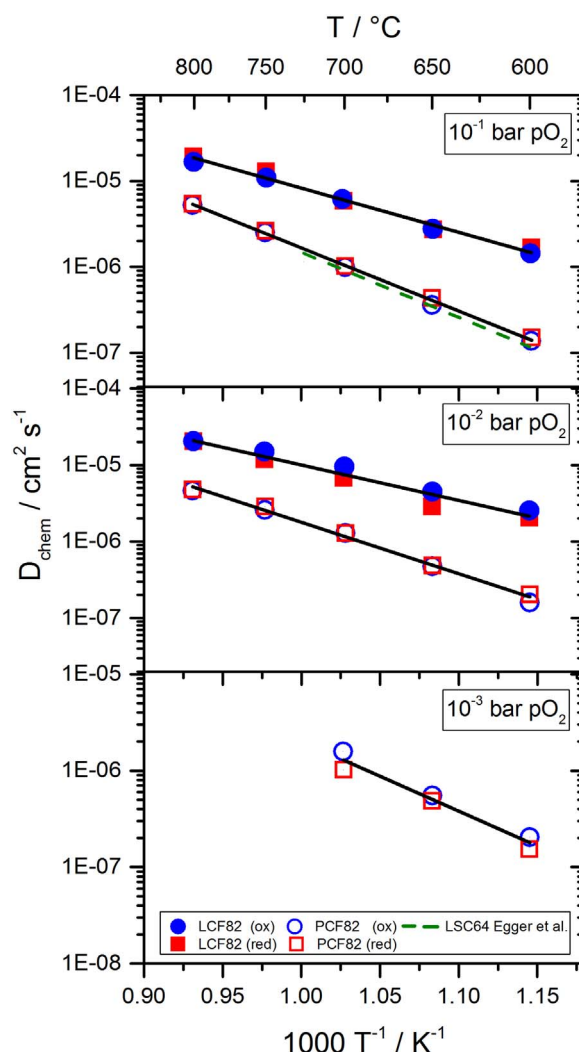


Fig. 6. Arrhenius plots of the chemical diffusion coefficients of oxygen (D_{chem}) of LCF82 (solid symbols) and PCF82 (open symbols) at different oxygen partial pressures; the twofold sigma standard deviation of multiple measurements is close to the size of the symbols. For comparison, data of LSC64 from Egger et al. [88] are given (dashed line). Activation energies for D_{chem} of LCF82 and PCF82 are summarized in Table 3. The activation energy for LSC64 at 10^{-1} bar $p\text{O}_2$ is 129 kJ mol^{-1} [88].

the determination of D_{chem} was not possible for LCF82 at $p\text{O}_2 = 1 \times 10^{-3}$ bar. LCF82 exhibits the highest value for $D_{\text{chem}} = 2 \times 10^{-5} \text{ cm}^2 \text{ s}^{-1}$ at 800 °C and $p\text{O}_2 = 0.1$ bar, whereas the value of PCF82 is approximately one order of magnitude lower than that of LCF82.

Cherry et al. [89] performed theoretical calculations on the dependence of ionic radius and migration energies in orthorhombic perovskites with various A-site elements. They concluded that perovskites substituted with smaller A-site cations, for instance Ca^{2+} , exhibit lower migration energies, and therefore faster oxygen diffusion. This trend agrees with the measured chemical diffusion coefficients of oxygen of LCF82 and PCF82 (Fig. 6), which show lower activation energies (Table 3) and faster oxygen diffusion, compared to state-of-the-art SOFC cathodes like $\text{La}_{0.6}\text{Sr}_{0.4}\text{CoO}_{3-\delta}$ (LSC64).

The activation energies E_a for k_{chem} and D_{chem} of LCF82 and PCF82 are given in Table 3. At high oxygen partial pressure (1×10^{-1} and 1×10^{-2} bar) E_a of both kinetic parameters is lower for LCF82 than for PCF82. At lower oxygen partial pressure, a higher activation energy is found for k_{chem} of LCF82 compared to PCF82.

Self-diffusion coefficients for oxygen, D_{O} , and self-diffusion coefficients for the oxygen vacancies, D_{V} , were estimated from the measured chemical diffusion coefficients by the relation $D_{\text{chem}} = \gamma_{\text{O}} D_{\text{O}}$, where γ_{O} is

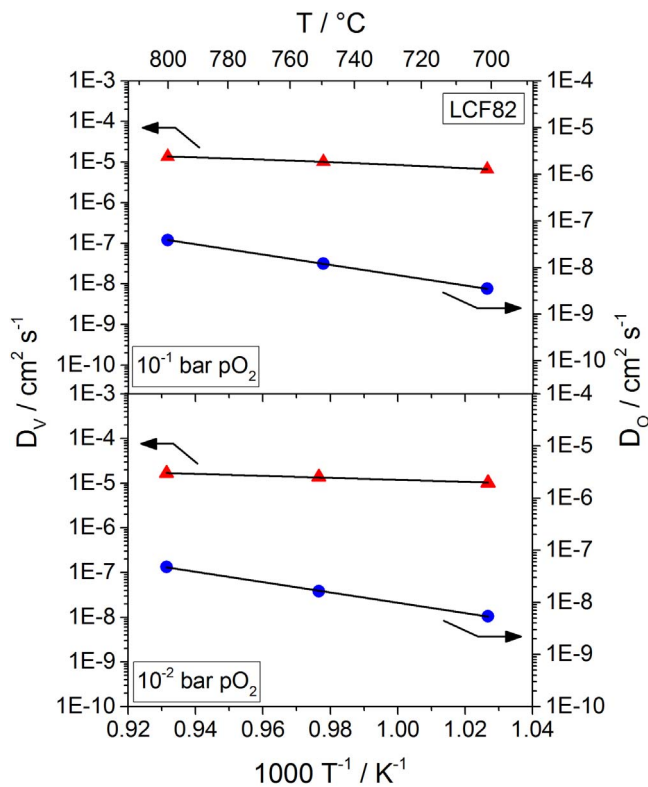


Fig. 7. Arrhenius plots of self-diffusion coefficients of oxygen (D_O) and oxygen vacancies (D_V) of LCF82 at different oxygen partial pressures.

the thermodynamic factor of oxygen, which is given by the following equation [90–92].

$$\gamma_O = \frac{1}{2} \left(\frac{\partial \ln p_{O_2}}{\partial \ln c_O} \right)_T = \frac{1}{2} \left(\frac{\partial \ln p_{O_2}}{\partial \ln (3-\delta)} \right)_T \quad (3)$$

The concentration of the oxygen ions, c_O was calculated from experimental data of the oxygen nonstoichiometry δ . Values for D_V can be calculated analogously from the relation $D_{chem} = \gamma_V D_V$, where γ_V is given by

$$\gamma_V = -\frac{1}{2} \left(\frac{\partial \ln p_{O_2}}{\partial \ln c_V} \right)_T = -\frac{1}{2} \left(\frac{\partial \ln p_{O_2}}{\partial \ln (3-\delta)} \right)_T \quad (4)$$

The thermodynamic factors of oxygen are in the range of 260–1750 for LCF82 (900–700 °C), and 700 for PCF82 (900 °C) (see also Fig. S-7 in the Supplementary material). The further analysis could only be performed for LCF82, due to lack of experimental data of the oxygen nonstoichiometry of PCF82 (compare Sections 3.2 and 3.3). Estimated values of the self-diffusion coefficients of LCF82 are plotted in Fig. 7, and activation energies for D_O and D_V are listed in Table 3. The oxygen vacancy diffusion coefficients of LCF82 are in good agreement with literature data of $La_{0.9}Ca_{0.1}FeO_{3-\delta}$ [34], $La_{1-x}Sr_xFeO_{3-\delta}$ ($x=0.1-0.5$) [4,47,90,93], and $La_{1-x}Sr_xCoO_{3-\delta}$ ($x=0.1-0.4$) [47,88]. In Fig. 8, oxygen surface exchange coefficients, k_O (estimated from $k_{chem} \approx k_O \gamma_O$), are given. The activation energies of k_O are listed in Table 3.

The ionic conductivities σ_{ion} of LCF82 were estimated via the Nernst-Einstein equation (neglecting contributions from the correlation factor and the Haven ratio) [88,94,95] at 700–800 °C for LCF82 (Fig. 9).

$$\sigma_{ion} = \frac{4 F^2 c_O D_O}{R T} \quad (5)$$

Ionic conductivities of LCF82 as measured by Bidrawn et al. [96] agree quite well with the estimated values from the present study. Zink et al. [31] also published data on the ionic conductivity of LCF82 which

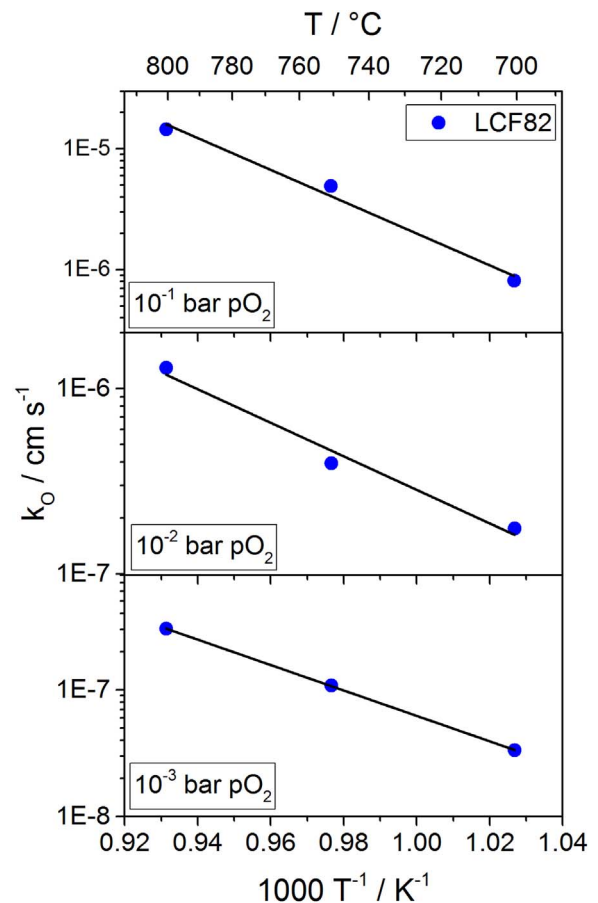


Fig. 8. Arrhenius plots of the surface exchange coefficient of oxygen of LCF82 at different oxygen partial pressures.

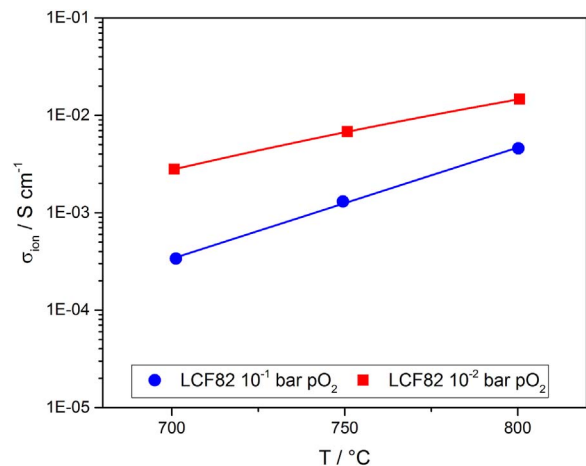


Fig. 9. Ionic conductivities of LCF82 as a function of temperature at different oxygen partial pressures; Lines are guides for the eye.

are approximately one order of magnitude higher than those we report here.

To study the possible oxygen migration pathways computationally, first the different O sites of the structures had to be determined. The oxygen vacancy formation energies, E_{vac} , can be expressed by

$$E_{vac} = E_{ACF_{3-x}} + \frac{1}{2} E_{O_2} - E_{ACF} \quad (6)$$

where $E_{ACF_{3-x}}$ is the total energy of the oxygen vacant supercell, while E_{ACF} is that of the stoichiometric supercell and E_{O_2} is the energy of an isolated oxygen molecule in the gas phase calculated in a $8 \times 8 \times 8$ Å

Table 4

Oxygen vacancy formation energies of the 80 atoms supercell of LCF and PCF at 1000 K and at 0 K (in parentheses).

| O site | LCF E_{vac} / eV | PCF E_{vac} / eV |
|--------|-----------------------|-----------------------|
| V1 | 2.43 (3.49) | 2.33 (3.50) |
| V2 | 2.49 (3.63) | 2.45 (3.65) |
| V3 | 2.44 (3.44) | 2.29 (3.44) |
| V4 | 2.42 (3.50) | 2.35 (3.53) |

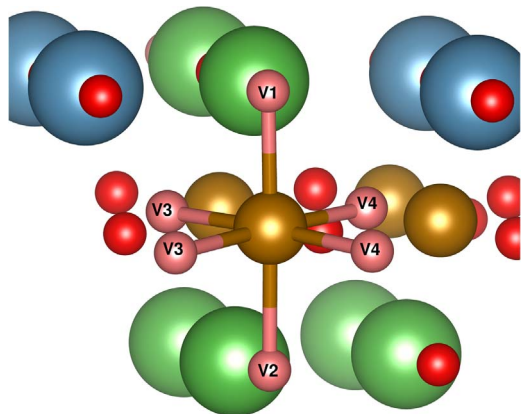


Fig. 10. Different oxygen positions in the FeO_6 octahedron of the supercells of LCF and PCF used for DFT calculations, Fe=orange, oxygen=red, calcium=blue, La/Pr=green. (For interpretation of the references to color in this figure legend, the reader is referred to the web version of this article.)

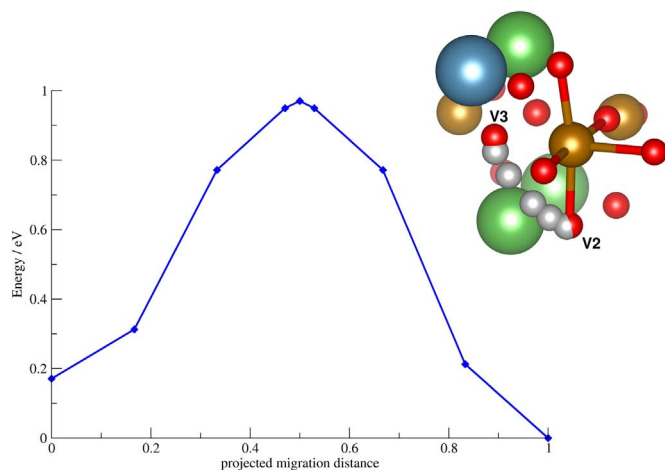


Fig. 11. A possible hopping route of oxygen (V2-V3) in LCF and its corresponding energy profile. The energy of the last image of the path was set 0.

simulation cell. According to the symmetry of the supercells, four different oxygen sites were expected and also confirmed by the calculation. The energies can be found in Table 4 ranging from 3.44 to 3.65 eV at 0 K and from 2.42 to 2.49 at 1000 K. In the literature, experimental values for similar perovskites ($\text{La}_{1-x}\text{Sr}_x\text{FeO}_{3-\delta}$) vary between 1 and 3.5 eV [39,40,97]. The positions of the O sites in the perovskite structures are shown in Fig. 10. The position closest to the rare earth layer, V2, shows significantly higher vacancy formation energy. It follows that the formation energy is dependent on the influence of the calcium atom on the oxygen position with respect to the arrangement within the structure.

The oxygen migration along the octahedron edges was investigated for LCF. Due to the four different octahedron positions, there are seven possible migration pathways, which are listed in Table S-5

(Supplementary material) with their corresponding activation energy. The Cl-NEB method predicted curved pathways with the energy maximum midway between the two oxygen sites. A possible hopping route as well as its corresponding energy profile is shown in Fig. 11. Difference in vacancy formation between the O sites causes asymmetric migration energies, whereas for Path 3 and Path 7 the energies are symmetrical around the hopping routes. The larger migration energy defines the rate-determining step of each path. In accordance with the experimental data of LCF82 (Table 3, activation energies of D_0 , which are between 82 and 92 kJ mol^{-1} depending on oxygen partial pressure), migration energies between 66.5 and 132.8 kJ mol^{-1} were calculated.

4. Conclusions

Two calcium acceptor-doped perovskites, $\text{La}_{0.8}\text{Ca}_{0.2}\text{FeO}_{3-\delta}$ (LCF82) and $\text{Pr}_{0.8}\text{Ca}_{0.2}\text{FeO}_{3-\delta}$ (PCF82), were synthesized and characterized with respect to their material properties like crystal structure, thermal expansion coefficients, and phase stability, as well as their oxygen exchange kinetics and mass and charge transport properties (surface exchange coefficient, chemical diffusion coefficient of oxygen, electronic and ionic conductivities). The thermal expansion coefficients of both LCF82 and PCF82 are in good agreement with those of state-of-the-art solid electrolytes. LCF82 exhibits electronic conductivities of $> 100 \text{ S cm}^{-1}$, whereas those of PCF82 are lower ($> 50 \text{ S cm}^{-1}$). Chemical surface exchange coefficients and chemical diffusion coefficients of oxygen were determined for both materials at 600–800 °C and $p\text{O}_2 = 0.1 - 1 \times 10^{-3}$ bar, respectively. LCF82 exhibits very high values of k_{chem} at $p\text{O}_2 = 0.1$ bar, whereas PCF82 provides faster exchange kinetics at lower oxygen partial pressures ($0.01 - 1 \times 10^{-3}$ bar). The chemical diffusion coefficients of LCF82 are approximately one order of magnitude higher than those of PCF82. The kinetic parameters of both LCF82 and PCF82 are higher than those of state-of-the-art SOFC cathode materials like $\text{La}_{0.6}\text{Sr}_{0.4}\text{CoO}_{3-\delta}$. Further, LCF82 shows good ionic conductivities at 700–800 °C. Due to these results, LCF82 and PCF82 are considered promising materials for air electrodes in SOFCs and SOECs. However, further investigations on the long-term stability of these materials should be performed under application relevant conditions (humid atmospheres, presence of Cr and Si impurities). The computational and experimental results agree well, independently confirming each other. Thus, calculations may be helpful in supporting experimental studies of further perovskites, especially of those which are more difficult to prepare and investigate experimentally.

Acknowledgements

Financial support by the Austrian 'Klima- und Energiefonds' and AVL List GmbH (Austria) within the program 'Mobilität der Zukunft' (project no. 845334, project title ASYSII) is gratefully acknowledged. Furthermore, the authors would like to thank V. Terziyska from Montanuniversitaet Leoben for XRD measurements and Grygoriy Dolgonos from Karl-Franzens-Universität Graz for useful discussions.

Appendix A. Supplementary material

Supplementary data associated with this article can be found in the online version at doi:10.1016/j.jssc.2017.12.019.

References

- [1] F. Ramadhani, M.A. Hussain, H. Mokhlis, S. Hajimolana, *Renew. Sustain. Energy Rev.* 76 (2017) 460–484.
- [2] A. Choudhury, H. Chandra, A. Arora, *Renew. Sustain. Energy Rev.* 20 (2013) 430–442.
- [3] N. Mahato, A. Banerjee, A. Gupta, S. Omar, K. Balani, *Progress Mater. Sci.* 72 (2015) 141–337.
- [4] J. Yoo, A. Verma, S. Wang, A.J. Jacobson, *J. Electrochem. Soc.* 152 (2005)

- A497–A505.
- [5] K.-D. Kreuer, Fuel Cells - Selected Entries from the Encyclopedia of Sustainability Science and Technology, 1st ed., Springer-Verlag, New York, 2013.
 - [6] K. Kendall, M. Kendall, High-temperature Solid Oxide Fuel Cells for the 21st Century, Academic Press, Oxford, UK, 2016.
 - [7] S.P. Simner, J.F. Bonnett, N.L. Canfield, K.D. Meinhardt, J.P. Shelton, V.L. Sprenkle, J.W. Stevenson, J. Power Sources 113 (2003) 1–10.
 - [8] A. Mai, V.A.C. Haanappel, S. Uhlenbruck, F. Tietz, D. Stöver, Solid State Ion. 176 (2005) 1341–1350.
 - [9] J.M. Ralph, C. Rossignol, R. Kumar, J. Electrochem. Soc. 150 (2003) A1518–A1522.
 - [10] W. Wang, Y. Huang, S. Jung, J.M. Vohs, R.J. Gorte, J. Electrochem. Soc. 153 (2006) A2066–A2070.
 - [11] W. Preis, E. Bucher, W. Sitte, Solid State Ion. 175 (2004) 393–397.
 - [12] O. Bartels, K.D. Becker, E. Bucher, W. Sitte, Solid State Ion. 177 (2006) 1677–1680.
 - [13] E. Bucher, W. Sitte, J. Electroceram. 13 (2004) 779–784.
 - [14] J. Mizusaki, T. Sasamoto, W.R. Cannon, H.K. Bowen, J. Am. Ceram. Soc. 66 (1983) 247–252.
 - [15] J. Mizusaki, M. Yoshihiro, S. Yamauchi, K. Fueki, J. Solid State Chem. 58 (1985) 257–266.
 - [16] E. Bucher, Department of General, Analytical, and Physical Chemistry (Ph.D. Thesis), Montanuniversität Leoben, Austria, Leoben, 2003.
 - [17] T. Horita, H. Kishimoto, K. Yamaji, M.E. Brito, T. Shimonosono, D. Cho, M. Izuki, F. Wang, H. Yokokawa, in: S.C. Singhal, K. Eguchi (Eds.), 12th Intern. Symp. Solid Oxide Fuel Cells (SOFC-XII), The Electrochemical Society, Pennington, USA, Montréal, Canada, 2011, pp. 511–517.
 - [18] H. Yokokawa, H. Tu, B. Iwanschitz, A. Mai, J. Power Sources 182 (2008) 400–412.
 - [19] N.H. Menzler, A. Mai, D. Stöver, Durability of cathodes including Cr poisoning, in: W. Vielstich, H. Yokokawa, H.A. Gasteiger (Eds.), Handbook of Fuel Cells - Fundamentals, Technology and Applications, John Wiley & Sons, Ltd., 2009, pp. 566–578.
 - [20] W. Araki, M. Miyashita, Y. Arai, Solid State Ion. 290 (2016) 18–23.
 - [21] R.D. Shannon, Acta Cryst. A 32 (1976) 751–767.
 - [22] N. Schrödl, E. Bucher, A. Egger, P. Kreiml, C. Teichert, T. Höschen, W. Sitte, Solid State Ion. 276 (2015) 62–71.
 - [23] N. Schrödl, E. Bucher, C. Gspan, A. Egger, C. Ganser, C. Teichert, F. Hofer, W. Sitte, Solid State Ion. 288 (2016) 14–21.
 - [24] M. Perz, E. Bucher, C. Gspan, J. Waldhäusl, F. Hofer, W. Sitte, Solid State Ion. 288 (2016) 22–27.
 - [25] T.C. Geary, S.B. Adler, Solid State Ion. 253 (2013) 88–93.
 - [26] R. Andoulsi, K. Horchani-Naifer, M. Férid, Powder Technol. 230 (2012) 183–187.
 - [27] R. Andoulsi, K. Horchani-Naifer, M. Férid, Ceram. Int. 39 (2013) 6527–6531.
 - [28] G. Pecchi, M.G. Jiliberto, A. Buljan, E.J. Delgado, Solid State Ion. 187 (2011) 27–32.
 - [29] R. Pushpa, D. Daniel, D.P. Butt, Solid State Ion. 249–250 (2013) 184–190.
 - [30] P. Ciambelli, S. Cimino, L. Lisi, M. Faticanti, G. Minelli, I. Pettiti, P. Porta, Appl. Catal. B: Environ. 33 (2001) 193–203.
 - [31] P.A. Zink, K.J. Yoon, U.B. Pal, S. Gopalan, Electrochem. Solid-State Lett. 12 (2009) B141–B143.
 - [32] Y. Nagata, S. Yashiro, T. Mitsuhashi, A. Koriyama, Y. Kawashima, H. Samata, J. Magn. Magn. Mater. 237 (2001) 250–260.
 - [33] S.K. Pandey, R. Bindu, P. Bhatt, S.M. Chaudhari, A.V. Pimpale, Physica B: Condens. Matter 365 (2005) 47–54.
 - [34] C. Berger, E. Bucher, W. Sitte, Solid State Ion. 299 (2017) 46–54.
 - [35] C. Berger, E. Bucher, C. Gspan, A. Menzel, W. Sitte, J. Electrochem. Soc. 164 (2017) F3008–F3018.
 - [36] K.T. Lee, A. Manthiram, J. Electrochem. Soc. 153 (2006) A794–A798.
 - [37] J.M. Serra, V.B. Vert, M. Betz, V.A.C. Haanappel, W.A. Meulenbergh, F. Tietz, J. Electrochem. Soc. 155 (2008) B207–B214.
 - [38] K. Kammer, Solid State Ion. 177 (2006) 1047–1051.
 - [39] A.M. Ritzmann, A.B. Muñoz-García, M. Pavone, J.A. Keith, E.A. Carter, Chem. Mater. 25 (2013) 3011–3019.
 - [40] H.-Y. Su, K. Sun, J. Mater. Sci. 50 (2015) 1701–1709.
 - [41] D. Maiti, Y.A. Daza, M.M. Yung, J.N. Kuhn, V.R. Bhethanabotla, J. Mater. Chem. A 4 (2016) 5137–5148.
 - [42] L. Lutterotti, Nucl. Inst. Methods Phys. Res., B (2010) 334–340.
 - [43] M.V. Patrakeev, J.A. Bahteeva, E.B. Mitberg, I.A. Leonidov, V.L. Kozhevnikov, K.R. Poeppelmeier, J. Solid State Chem. 172 (2003) 219–231.
 - [44] W. Preis, M. Holzinger, W. Sitte, Monatshefte Chem. 132 (2001) 499–508.
 - [45] M.W. den Otter, H.J.M. Bouwmeester, B.A. Boukamp, H. Verweij, J. Electrochem. Soc. 148 (2001) J1–J6.
 - [46] W. Preis, E. Bucher, W. Sitte, J. Power Sources 106 (2002) 116–121.
 - [47] T. Ishigaki, S. Yamauchi, K. Kishio, J. Mizusaki, K. Fueki, J. Solid State Chem. 73 (1988) 179–187.
 - [48] VASP TST Tools, (<http://theory.cm.utexas.edu/vtsttools/12.01>).
 - [49] G. Kresse, J. Hafner, Phys. Rev. B 48 (1993) 13115–13118.
 - [50] G. Kresse, J. Furthmüller, Phys. Rev. B 54 (1996) 11169–11186.
 - [51] G. Kresse, J. Furthmüller, Comput. Mater. Sci. 6 (1996) 15–50.
 - [52] G. Kresse, D. Joubert, Phys. Rev. B 59 (1999) 1758–1775.
 - [53] J.P. Perdew, K. Burke, M. Ernzerhof, Phys. Rev. Lett. 77 (1996) 3865–3868.
 - [54] S. Grimme, J. Antony, S. Ehrlich, H. Krieg, J. Chem. Phys. 132 (2010) 154104.
 - [55] S. Grimme, S. Ehrlich, L. Goerigk, J. Comput. Chem. 32 (2011) 1456–1465.
 - [56] H. Jónsson, G. Mills, K.W. Jacobsen, Nudged elastic band method for finding minimum energy paths of transitions, classical and quantum dynamics in condensed phase simulations, World Sci. (2011) 385–404.
 - [57] G. Henkelman, B.P. Uberuaga, H. Jónsson, J. Chem. Phys. 113 (2000) 9901–9904.
 - [58] G. Henkelman, H. Jónsson, J. Chem. Phys. 113 (2000) 9978–9985.
 - [59] J.M. Huidspeth, G.A. Stewart, A.J. Studer, D.J. Goossens, J. Phys. Chem. Solids 72 (2011) 1543–1547.
 - [60] T. Sato, S. Takagi, S. Deledda, B.C. Hauback, S.-i. Orimo, Sci. Rep. 6 (2016) 23592.
 - [61] Y. Ren, R. Küngas, R.J. Gorte, C. Deng, Solid State Ion. 212 (2012) 47–54.
 - [62] H.M. Taguchi, Y. Hirota, K. Yamaguchi, O. Mat. Res. Bull. 40 (2005) 773–780.
 - [63] P.M. Price, E. Rabenberg, D. Thomsen, S.T. Mixture, D.P. Butt, J. Am. Ceram. Soc. 97 (2014) 2241–2248.
 - [64] S.J. Hong, A.V. Virkar, J. Am. Ceram. Soc. 78 (1995) 433–439.
 - [65] N.Q. Minh, T. Takahashi, Chapter 4 - Electrolyte, in: N.Q.M. Takahashi (Ed.) Science and Technology of Ceramic Fuel Cells, Elsevier Science Ltd, Oxford, 1995, pp. 69–116.
 - [66] T. Ishihara, N.P. Bansal (Ed.) Fuel Cells and Hydrogen Energy, Springer, New York, 2009.
 - [67] V.V. Kharton, A.A. Yaremchenko, E.N. Naumovich, J. Solid State Electrochem. 3 (1999) 303–326.
 - [68] M.-H. Hung, M.V.M. Rao, D.-S. Tsai, Mater. Chem. Phys. 101 (2007) 297–302.
 - [69] W. Sitte, E. Bucher, W. Preis, Solid State Ion. 154–155 (2002) 517–522.
 - [70] A.N. Petrov, V.A. Cherepanov, O.F. Kononchuk, L.Y. Gavrilova, J. Solid State Chem. 87 (1990) 69–76.
 - [71] E. Bucher, Habilitation Thesis, Chair of Physical Chemistry, Montanuniversität Leoben, Leoben, 2013.
 - [72] J. Mizusaki, Y. Mima, S. Yamauchi, K. Fueki, H. Tagawa, J. Solid State Chem. 80 (1989) 102–111.
 - [73] V.V. Kharton, A.V. Kovalevsky, M.V. Patrakeev, E.V. Tsipis, A.P. Viskup, V.A. Kolotygin, A.A. Yaremchenko, A.L. Shaula, E.A. Kiselev, J.C. Waerenborgh, Chem. Mater. 20 (2008) 6457–6467.
 - [74] L.-W. Tai, M.M. Nasrallah, H.U. Anderson, D.M. Sparlin, S.R. Sehlin, Solid State Ion. 76 (1995) 259–271.
 - [75] L.-W. Tai, M.M. Nasrallah, H.U. Anderson, D.M. Sparlin, S.R. Sehlin, Solid State Ion. 76 (1995) 273–283.
 - [76] T. Montini, M. Bevilacqua, E. Fonda, M.F. Casula, S. Lee, C. Tavnagnacco, R.J. Gorte, P. Fornasiero, Chem. Mater. 21 (2009) 1768–1774.
 - [77] S. Uhlenbruck, F. Tietz, Mater. Sci. Eng.: B 107 (2004) 277–282.
 - [78] S. Yamaguchi, Y. Okimoto, Y. Tokura, Phys. Rev. B 54 (1996) R11022–R11025.
 - [79] J.S. Zhou, J.B. Goodenough, Phys. Rev. B 69 (2004) 153105.
 - [80] J.S. Zhou, J.B. Goodenough, Phys. Rev. Lett. 94 (2005) 065501.
 - [81] J.B. Goodenough, J.S. Zhou, J. Mater. Chem. 17 (2007) 2394–2405.
 - [82] J.S. Zhou, J.B. Goodenough, Phys. Rev. B 77 (2008) 132104.
 - [83] M. Søgaard, P. Vang Hendriksen, M. Mogensen, J. Solid State Chem. 180 (2007) 1489–1503.
 - [84] M.V. Patrakeev, I.A. Leonidov, V.L. Kozhevnikov, K.R. Poeppelmeier, J. Solid State Chem. 178 (2005) 921–927.
 - [85] H.W. Brinks, H. Fjellvåg, A. Kjekshus, B.C. Hauback, J. Solid State Chem. 150 (2000) 233–249.
 - [86] J.E. ten Elshof, H.J.M. Bouwmeester, H. Verweij, Solid State Ion. 81 (1995) 97–109.
 - [87] M.A. Tamimi, A.C. Tomkiewicz, A. Hug, S. McIntosh, J. Mater. Chem. A 2 (2014) 18838–18847.
 - [88] A. Egger, E. Bucher, M. Yang, W. Sitte, Solid State Ion. 225 (2012) 55–60.
 - [89] M. Cherry, M.S. Islam, C.R.A. Catlow, J. Solid State Chem. 118 (1995) 125–132.
 - [90] J.E. ten Elshof, M.H.R. Lankhorst, H.J.M. Bouwmeester, J. Electrochem. Soc. 144 (1997) 1060–1067.
 - [91] J.A. Lane, S.J. Benson, D. Waller, J.A. Kilner, Solid State Ion. 121 (1999) 201–208.
 - [92] R. Merkle, J. Maier, J. Fleig, Mechanistic understanding and electrochemical modeling of mixed conducting (SOFC) electrodes, in: W. Vielstich, H. Yokokawa, H.A. Gasteiger (Eds.), Handbook of Fuel Cells - Fundamentals, Technology and Applications, John Wiley & Sons, Ltd., 2009, pp. 425–440.
 - [93] M. Søgaard, P.V. Hendriksen, M. Mogensen, J. Solid State Chem. 180 (2007) 1489–1503.
 - [94] E. Bucher, A. Egger, P. Ried, W. Sitte, P. Holtappels, Solid State Ion. 179 (2008) 1032–1035.
 - [95] V.V. Vashook, M. Al Daroukh, H. Ullmann, Ionics 7 (2001) 59–66.
 - [96] F. Bidrawn, S. Lee, J.M. Vohs, R.J. Gorte, J. Electrochem. Soc. 155 (2008) B660–B665.
 - [97] Y.A. Mastrikov, R. Merkle, E.A. Kotomin, M.M. Kuklja, J. Maier, Phys. Chem. Chem. Phys. 15 (2013) 911–918.